Combining paleomagnetic and Re–Os isotope data to date hydrocarbon generation and accumulation processes

Jing Hu[1], Yong Zhang[2]*, Dong Jia[1]*, Adrian Muxworthy[3,4], David Selby[5], Yongxiang Li[1], Matthew J. Brzozowski[6], Guoqi Wei[7], Jian Cao[1], Hongwei Yin[1], Wei Li[2]

[1]State Key Laboratory for Mineral Deposits Research and Department of Earth Sciences, Nanjing University, Nanjing, 210046, China

[2]Nanjing Institute of Geology and Palaeontology, Chinese Academy of Sciences, Nanjing, 210008, China

[3]Department of Earth Science and Engineering, Imperial College London, London, SW7 2AZ, UK

[4]Department of Earth Sciences, University College London, London, WC1E 6BT, UK.

[5]Department of Earth Sciences, University of Durham, Durham, DH1 3LE, UK

[6]Department of Geology, Lakehead University, Thunder Bay, Ontario, P7B 5E1, Canada,

[7]Research Institute of Petroleum Exploration and Development, PetroChina, Beijing, 100083, China

Corresponding authors: Yong Zhang (yzhang@nigpas.ac.cn); Dong Jia (djia@nju.edu.cn)

Key Points:

- Palaeomagnetic and Re–Os isotope data were collected for a hydrocarbon carbonate reservoir to determine the hydrocarbon evolution processes.

- Oil accumulations are found to have remagnetized the reservoir carbonates during the Late Triassic and Cretaceous.

- Timing of oil generation is constrained by Re–Os dates of bitumen and oil hosted in carbonates at ~264 and ~94 Ma, respectively.

Abstract

Unravelling the complex relationship between orogenesis and hydrocarbon formation and accumulation is challenging and is often hampered by physical and chemical overprints of younger events. The Permian reservoir in the Longmen Shan orogen, South China, is such an example, and its evolution has been hotly debated. In this study, we use a new combination of paleomagnetic dating analysis and Re–Os isotope dating to try to resolve this. Paleomagnetic dating of the hydrocarbon-host carbonate indicates two remagnetization events during: (1) the Late Triassic, and (2) the Middle Jurassic–Cretaceous. These two remagnetization events are shown to represent two distinct stages of hydrocarbon accumulation. The paleomagnetic estimates are supported by Re–Os dating of bitumen (~264 Ma) and oil (~94 Ma). The two different Re–Os ages are associated with two periods of oil generation. We interpret these data in terms of known geological processes: (1) the ~260 Ma Dongwu large igneous province caused oil generation, and the Indosinian tectonic event caused the migration and accumulation; and (2) the Late Cretaceous Yanshan orogenic events promoted another generation and entrapment of oil in the same reservoir. This combined approach reliably tracks the sequence of oil generation and accumulation, even when the source rock is uncertain, and multi-phase accumulation and complex tectonism has occurred. Given that paleomagnetic and Re–Os dating are independent methods which can constrain multiple geological processes, when used together they have the potential to be universally applied.

Plain Language Summary.

Key to understanding complex geological processes is the dates and sequence of each event. The timing of hydrocarbon formation and accumulation is one such complex geological process that can be difficult to unravel, but critical to evaluate the complex orogenesis and hydrocarbon explorations. In this paper, we combine for the first time two independent dating methods to study hydrocarbon reservoirs of Longmen Shan orogen: (1) paleomagnetic and (2) rhenium–osmium isotope dating. The two methods identified two periods of hydrocarbon formation, followed by two extended periods of hydrocarbon migration. This combined method is particularly powerful as it is independent of the hydrocarbon source rock and complex geological settings. Moreover, the two methods can provide additional tests for each dating technique. The new combined methods can, therefore, be applied in complex hydrocarbon-bearing regions worldwide.

1 Introduction

Determining the spatial and temporal evolution of hydrocarbon reservoir systems helps us to improve yield from mature reservoir systems, thus reducing the need for further exploration as the world moves towards a carbon-free future. The evolution of such hydrocarbon systems can be problematic due to a number of processes, which can contribute to, for example, the maturation history of the source rocks, oil migration and accumulation patterns, hydrocarbon cracking or gas generation in reservoir rocks, and the destruction of hydrocarbon reservoir systems (e.g., Zhang et al., 2018, 2019).

Key to understanding hydrocarbon reservoir evolution is quantifying the timing of formation of the hydrocarbon and reservoir itself (Bhullar et al., 1999). There is no single method that consistently yields correct ages for hydrocarbon and reservoir formation. We propose combining two different complementary methods for determining hydrocarbon evolution ages: (1) paleomagnetic dating methods, and (2) Re–Os geochronology. Paleomagnetic dating has previously been carried out on hydrocarbon-bearing rocks to provide time ranges of hydrocarbon generation, accumulation, and destruction (Elmore et al., 1987; Elmore & Leach, 1990; Zhang et al., 2016, 2018, 2019). This method requires isolation of the characteristic remanent magnetization (ChRM), assuming hydrocarbon activities are related to remagnetization, and then comparison with the apparent polar wander paths (APWP) of the region. Given the availability of quantitative relationships between magnetic and hydrocarbon parameters, paleomagnetic ages can often be directly linked to hydrocarbon evolution processes (e.g., Manning & Elmore, 2015; Zhang et al., 2016). However, the effectiveness of this method is limited by the accuracy of published APWP paths. Rhenium–osmium (Re-Os) geochronology can be applied directly to crude oil and bitumen in reservoir rocks to determine absolute ages (Georgiev et al., 2016; Selby et al., 2005). Interpreting these ages in the context of geological processes is often difficult, however, as the hydrocarbon undergoes continuous modifications, which could modify the Re–Os systematics throughout the petroleum history (Ge et al., 2016; Li et al., 2017; Lillis & Selby, 2013). By combining these two entirely independent methods we aim to compensate for each methods' limitations, allowing for temporal variations in hydrocarbon evolution to be more accurately dated.

To determine the effectiveness of these combined approaches, we used paleomagnetic and Re–Os dating methods to study the Longmen Shan foreland thrust belt in South China (Figure 1), which contains a complex hydrocarbon system in its northern part (Jia et al., 2006). The generation and migration history of the hydrocarbons is uncertain. They may be the product of several accumulation processes, and have been affected by multiple tectonic events since the Ediacaran, including the Dongwu large igneous province and Caledonian, Indosinian, Yanshan and Himalayan orogenies (Figure 1d; Jia et al., 2006). In addition to paleomagnetic and Re–Os dating, we also measured the total organic carbon (TOC) content, bitumen reflectance and $^{87}Sr/^{86}Sr$ isotope ratios to better characterize the relationship between the remagnetization and hydrocarbon activities.

2 Geological Setting

The Longmen Shan foreland thrust belt is on the western boundary of the Sichuan Basin close to the Tibetan Plateau. It is marked by a NE striking thrust belt with fault-related folds and the western Sichuan foreland basin (Burchfiel et al., 1995; Jia et al., 2006; Figure 1a–c). Multiple tectonic events have happened in this area from the Permian to present, including the Dongwu large igneous province, and the Indosinian, Yanshan, and Himalayan orogenies (Figure 1d). The ~260 Ma Dongwu large igneous province relates to the mantle plume which produced the extensive Emeishan flood basalts around the Sichuan Basin, and the unconformities in the Middle Permian strata (He et al., 2007; Shellnutt, 2014). Subsequently, due to the closure of the Paleotethys between the South China, North China, and Qiangtang continental blocks, the Late Triassic Indosinian orogeny initiated deformation of the Longmen Shan belt (Jia et al., 2006; Figure 1b). Meanwhile, Late Triassic Sichuan foreland basin formed in the eastern part of Longmen Shan belt because of tectonic loading (Jia et al., 2006; Zhang et al., 2015a; Figure 1c). The subsequent Yanshan orogeny, which occurred during Jurassic–Cretaceous in this region, is the result of the East Asian and Siberia continent-continent collision and subduction of paleo-Pacific plate (Dong et al., 2018). The Yanshan orogeny was tectonically relatively quiet, generally lacking intense deformation. However, some unconformities, metamorphism and igneous intrusions indicate that thrusting occurred; there was slow uplift of the Longmen Shan thrust belt and the continuous subsidence of the adjacent foreland basin (Li et al., 2012). The Cenozoic Himalayan orogeny resulting from the India-Asia collision is the most recent event recorded in this region (Yan et al., 2011, 2018). During this event, the present Longmen Shan belt formed through rapid uplift, exhumation and deformation (Li et al., 2014; Wang et al., 2012).

The Permian marine carbonate rocks in the Sichuan Basin are one of the most important reservoir rocks in South China as they host the largest gas field of China — the Puguang gas field in the eastern Sichuan Basin (Figure 1b). These reservoir rocks are well exposed in the northern portion of the Longmen Shan belt (Figure 1), and comprise dolostone and bioclastic limestone of the Qixia Formation, and limestone of the Maokou Formation (Figure 1d). However, the superimposed tectonism mentioned above, results in a complex hydrocarbon system, whose formation is a matter of debate. For example, the hydrocarbon source rock has been proposed to be: (1) the black shales of the lower Cambrian strata (Tan et al., 2022), (2) the Permian rocks in the region (Gao et al., 2020), (3) Silurian source rocks in other regions (Xie et al., 2020), or (4) a mixture of these (Hu et al., 2021). Additionally, a wide range of hydrocarbon generation and accumulation dates have been proposed primarily from basin modeling, with no consensus, for example, the Permian (Qiu et al., 2021), Triassic–Jurassic (Li et al., 2022), the Cretaceous (Luo et al., 2020) and the Paleogene (Lu et al., 2017).

3 Samples and Methods

3.1 Paleomagnetism

To characterize the remagnetization of the Permian reservoir, 182 hydrocarbon-bearing carbonate samples were collected from 23 sites distributed along both limbs of three folds in the thrust belt, i.e., the Zhuyuan, Changjianggou, and Chejiaba folds (Figure 1). Samples were either demagnetized thermally in an ASC TD–48 thermal demagnetizing oven at steps of 20–50°C to a maximum temperature of 570°C, or demagnetized in an alternating field (AF) at steps of 3–10 mT to a maximum of 100 mT. Magnetic measurements were conducted using a 2G-755 cryogenic rock magnetometer in the magnetic shielded room of Nanjing University. Orthogonal-projection plots were used to identify ChRM directions using a principal-component analysis of Kirschvink (1980) and software of Enkin (1994). For constraining the ages of the ChRMs with respect to folding, the fold test and progressive-tilt tests were applied (Enkin, 2003; Tauxe & Watson, 1994; Tauxe et al., 2016).

3.2 Rock magnetic analysis

For estimating the magnetic mineralogy and the magnetic-minerals' grain-size distribution, isothermal remanent magnetization (IRM) acquisition curves were measured on 16 representative specimens at the paleomagnetic laboratory of Nanjing University. The IRM acquisition curves were obtained using an impulse magnetizer (ASC IM–10–30) and a spinner magnetometer (AGICO JR–6A). The unmixing methods were used to analyze the results (Kruiver et al., 2001).

To better quantify the mineralogy, a 'Lowrie test' was conducted (Lowrie, 1990). The specimens were magnetized firstly along the z-axes using a field of 2.4 T, and then along y-axes with a field of 0.4 T and ultimately along x- axes using a field of 0.12 T. The samples were then heated to 680°C during stepwise thermal demagnetization.

3.3 Re–Os isotopes

Re–Os analysis was conducted to determine the ages of hydrocarbon formation. We undertook Re–Os analysis on four oil and eleven bitumen samples from reservoir carbonate rocks where paleomagnetic measurements were done, i.e., oil from the Zhuyuan fold, and bitumen from the Changjianggou and Chejiaba folds (Figure 1). At the Durham Geochemistry Centre laboratory, ~100 mg of oil and ~150 mg of bitumen were dissolved in Carius tubes using 6 ml HNO_3 and 3 ml HCl for 24 hours at 220°C, and then equilibrated by the given amount of ^{185}Re and ^{190}Os tracer solution. Chloroform and micro-distillation were used to extract and purify Os from the acid solution. Subsequently, the NaOH-acetone extraction and anion exchange chromatography were used to isolate the remaining Re bearing solution. The Ni and Pt filaments were applied to load the isolated Re and Os fractions, and the isotope ratios were measured via a Thermo Scientific TRITON-Electron mass spectrometer. Finally, Re–Os data were regressed via a toolkit (Isoplot V. 4.15) of Ludwig (2008) and a ^{187}Re decay constant (1.666×10^{-11} a^{-1}) of Smoliar et al. (1996).

3.4 Scanning electron microscopy (SEM)

For further identifying the magnetic remanence carriers, scanning electron microscopy (SEM) was used to image typical polished sections. This was done using a field–emission–gun scanning electron microscope (Supra-55 Sapphire) equipped with an energy dispersive spectrometer (Oxford Aztec X-Max 150) at Nanjing University. Backscatter-electron images were used to easily identify the iron oxides or sulfides, and energy-dispersive X-ray spectroscopy (EDS) to describe the elemental contributions.

3.5 The Analysis of Total Organic Content, Bitumen Reflectance in oil and Strontium Isotopes

To estimate the amount of hydrocarbon present in the samples, total organic content (TOC) was determined on 20 representative carbonate samples on which ChRMs were also determined. The bitumen reflectance (*Rob*) of five bitumen samples was measured to quantify maturity; this was accomplished at Nanjing University using an incident light microscope (Zeiss Axiokop 40 Pol) with a 50 × 0.85 oil immersion objective and at a wavelength of 546 nm. The *Rob* values were converted to the vitrinite reflectance (*Ro*) by using an equation $Ro = 0.618 \times Rob + 0.4$ of Jacob (1985).

To characterize the fluids that potentially caused the remagnetization, we measured strontium isotope ratios ($^{87}Sr/^{86}Sr$) of 14 representative hydrocarbon-bearing carbonate samples on a TRITON mass spectrometer at Nanjing University. The values were normalized relative to SRM 987 = 0.710250 (± 13) (SRM = standard reference material). In order to calculate Permian $^{87}Sr/^{86}Sr$ ratios from present-day values, the Sr concentration of the samples was measured using an inductively coupled-plasma mass spectrometer (Aurora M90).

4 Results

4.1 Paleomagnetic analysis

From thermal and AF demagnetization data, most samples yielded reliable remanence directions (Figure 2). A low temperature component was isolated < 250°C, which was similarly isolated for alternating fields <15 mT (Figures 2a and 2b). The site-mean direction of this component (Declination = 356°, Inclination = 51°, number of sites = 27, α_{95} = 3°) is similar to the present-day field. Higher-temperature components with direction differences were isolated between ~280°C and 370°C–480°C; there were corresponding components identified using AF demagnetization, i.e., AF = 15–50 mT. These components were the characteristic magnetizations, the ChRMs (Table 1). Two ChRMs were identified: (1) ChRM-1 was found in 13 sites, and is characterized by mean values of declination (*Dg*) = 41°, inclination (*Ig*) = 47° (α_{95} = 4°) in geographic coordinates, and a declination (*Ds*) = 43°, inclination (*Is*) = 48° (α_{95} = 20°) in stratigraphic coordinates (Figures 2c and 2e); (2) ChRM-2 was found in 10 sites, with a mean *Dg* = 18°, *Ig* = 48° (α_{95} = 4°) in geographic coordinates, and *Ds* = 44°, *Is* = 49° (α_{95} = 34°) in stratigraphic coordinates (Figures 2d and 2f). Most ChRM-1 directions occur in samples from the Chejiaba and Changjiagou folds, while most ChRM-2 occur in samples from the Zhuyuan fold. To constrain the ages of the ChRMs with respect to folding, a fold test and progressive tilt test were conducted. The results of the fold test are negative for the ChRMs (Figures 2c–f), suggesting that these carbonate rocks were remagnetized after the formation of the folds during the Triassic (Enkin, 2003; Tauxe et al., 2016; Tauxe & Watson, 1994). The progressive tilt test exhibits similar results, with maximum *K* values at 4.4% and 3.9% unfolding (Figure 3). The fold test of Tauxe and Watson (1994) show maximum *K* values at -3% ~8% unfolding for ChRM-1 and maximum *K* values at -1%~7% unfolding for ChRM-2 (Figure 4).

4.2 Rock magnetic analysis

Representative samples from different regions and lithology were chosen for IRM analysis, and typical curves are shown in Figure 5. Most samples show a typical curve of low to medium coercivity magnetic minerals, as they reach ~80% of saturation IRM before 0.2 T (Figures 5a and 5b). In contrast, two samples (CJG04 and CJG06; Figures 5b) did not reach saturation in a field of 1.0 T and 2.4 T, which is a characteristic of hard coercivity remanence carriers (e.g., Yang et al., 2004). To analyze the IRM acquisition curves, the unmixing approach of Kruiver et al. (2001) was applied (Figures 5c–h; Table S1). In this approach, the IRM acquisition curves are manually unmixed into components assuming lognormal distributions; the components are characterized by their mean coercivity ($B_{1/2}$), saturation IRM and half-width of the distribution (DP). For example, for sample CJG06 two components were identified. There is a 'hard' magnetic component with $B_{1/2}$ ~ 1737 mT and DP ~ 0.2, which potentially corresponds to hematite, and a 'soft' component (18%) with $B_{1/2}$ ~ 56 mT and DP ~ 0.36. Generally, for most samples two components were identified (e.g., CJB04 and CJB08 in Figures 5e and 5g): (1) a 'soft component' making up 65%–99% of IRM contributions with $B_{1/2}$ ~ 40 to 56 mT, and (2) a 'hard component' with $B_{1/2}$ ~ 501 to 2512 mT. The 'soft' component is indicative of a magnetite-like phase, and the 'hard' a hematite-like phase.

The samples were subjected to a 'Lowrie' test (Lowrie, 1990; Figure 6) to try to identify the magnetic mineralogy. Most samples were dominated by the soft fraction, demagnetizing between 400–570°C, and likely indicating magnetite. There was also a medium and hard fraction. For the samples CJB04 and CJB07, the unblocking temperatures of the hard fractions were ~680°C, indicating the presence of hematite. For the samples CJB04, CJB07 and ZY02, the soft or medium fractions at ~325°C suggest an iron-sulphide ferromagnetic (*s.l.*) phase likely pyrrhotite or greigite. For samples CJB08 and ZY02, the final demagnetization temperature of both medium and hard fractions was at ~350°C, indicating an absence of hematite in these samples.

4.3 Re–Os isotopes

The Re–Os isotopic analysis of oil and bitumen produced two sets of date results. The four oil samples contain between 8.4–46.8 ppb Re and 198.0–600.6 ppt Os, with $^{187}Re/^{188}Os$ and $^{187}Os/^{188}Os$ ratios of 194.8–562.7 and 1.29–1.87, respectively (Table 2). The Re–Os data of the oil samples produce a Model 3 date of 94 ± 10 Ma, with an initial $^{187}Os/^{188}Os$ value of 0.994 ± 0.061 (MSWD = 3.7; Figure 7a). The eleven bitumen samples contain 7.7–80.7 ppb Re and 97.3–669.0 ppt Os, with $^{187}Re/^{188}Os$ and $^{187}Os/^{188}Os$ ratios of 102.5–2903.6 and 2.3–15, respectively. The bitumen samples produce a Re–Os date of 268 ± 17 Ma (Model 3), with an initial $^{187}Os/^{188}Os$ value of 1.60 ± 0.35 (MSWD = 541; Figure 7b). The bitumen Re–Os date estimate does, however, have a large MSWD and a Model 3 fit, indicating that significant geological scatter exists in addition to analytical uncertainties (Ludwig, 2008). The bitumen originating from several different source rocks is suggested to be the primary cause of the scatter in the dataset, which resulted in large variation of initial $^{187}Os/^{188}Os$ ratios (Selby et al 2005). The initial $^{187}Os/^{188}Os$ ratios of 6 out of the 11 bitumen samples at 268 Ma are similar, ranging from 1.2 to 1.6 (samples Bitumen-1, 2, 4, 6, 7 and 9), indicative of a similar origin. This subset of samples produces a Re–Os date of 264 ± 16 Ma, with a lower degree of scatter (MSWD = 42; Figure 7b).

4.4 SEM analysis

SEM imaging found that the matrix for the reservoir rock is typically constituted by carbonate, fractures and pores (Figure 8). In most hydrocarbon-bearing samples, bitumen can be observed along the fractures or in the pores (Figures 8a–c); EDS analysis of the bitumen identified sulfur and carbon

(Figure 8g). Fine-grained iron oxides (generally <10 μm in diameter) occur as disseminated grains and framboidal clusters along bitumen-filled fractures and pores (Figure 8). Together with the rock magnetic results, most of these iron oxides are likely authigenic magnetite, although a few hematite grains may occur (Elmore et al., 1987, 2012). Iron sulfides can also be observed presented in framboidal forms in the matrix, some of which are not in the fractures. Together with the EDS analysis, most of the iron sulfides should be pyrite (Figures 8a and 8h), ferrimagnetic iron-sulfides may also be present (Figures 8f and 8j), e.g., greigite.

4.5 The analysis of Total Organic Content, Bitumen Reflectance in oil and Strontium Isotopes

A group of 20 hydrocarbon-bearing samples were selected for the TOC measurement. The values range from 0.01 to 0.78 wt. % (Table S2), and is positively correlated with the natural remanent magnetization (NRM) with a Pearson's correlation coefficient $R = 0.78$ (Figure 9). This phenomenon has been reported previously for hydrocarbon-rich rocks (Emmerton et al., 2012; 2013)

The vitrinite reflectance (Ro) was converted from bitumen reflectance, which was measured on five representative bitumen samples. The mean Ro values range from 0.9% to 1.2%, maximum Ro values range from 1.0% to 1.4%, and minimum Ro values from 0.7% to 0.9% (Table S3). Thirteen carbonate samples yielded $^{87}Sr/^{86}Sr$ ratios in a narrow range of 0.70704–0.70731, and the sample of ZY4-10 yielded a higher ratio of 0.70794 (Table S4). All of these values are inside the isotopic scope of contemporaneous Permian seawater (0.7070–0.7080) (McArthur et al., 2012; Figure 10).

5 Discussion

Based on the paleomagnetic demagnetization data, two ChRM directions were identified in the hydrocarbon-bearing carbonate samples from the northern portion of Longmen Shan belt. Fold tests suggest that both ChRMs were acquired post-folding. The ChRM directions are thought not to be the result of regional block rotations, due to the similarity between the primary geomagnetic result of Permian–lower Triassic strata in the studied region and those in the stable areas in South China (Heller et al 1988; Li & Wang, 1989; Steiner et al., 1989). Disregarding vertical axis rotations, a comparison of the paleopole determined from the ChRMs with the APWP of South China (Figure 2g) indicates that the two mean ChRM directions were acquired during two separate time periods, the Late Triassic and Middle Jurassic–Cretaceous. The ages of both ChRMs post-date the deposition of the hydrocarbon-bearing carbonate, which, together with the negative fold test results, indicates that both ChRMs are secondary remanent magnetizations. Based on the rock magnetism, the ChRMs are mainly carried by magnetite, which can be observed as authigenic magnetite in the back-scatter images. The evidence that the ChRMs are chemical remagnetizations is twofold: (1) the low vitrinite reflectance values of bitumen, i.e., 0.9–1.2%, indicate temperatures < 200°C, and (2) authigenic magnetite – the main carrier of the ChRMs – was widely observed within bitumen-filled fractures (Figure 8).

5.1 The origin of the remagnetization events in the reservoir carbonate

This remagnetization was most likely due to the migration and accumulation of hydrocarbon fluids within the Permian carbonates (Machel, 1995; Zhang et al., 2018). This argument is supported by three lines of evidence: (1) in the oil- and bitumen-rich carbonate rocks, authigenic magnetite was commonly

observed co-existing with hydrocarbons (Figure 8), (2) the Permian carbonate contains a high amount of oil and bitumen, with NRM intensities (a reflection of magnetite content) correlated with TOC (a reflection of the hydrocarbon content; Figure 9), and (3) the Sr isotope composition of the carbonate rocks indicate that they were not significantly altered by chemically evolved orogenic fluids (Figure 10). These three characteristics have previously been used to associate the acquisition of chemical remagnetization to hydrocarbon accumulation (Elmore et al., 1987; Elmore & Leach, 1990; Zhang et al., 2018). The same association can be employed here; we link the two remagnetization events to two stages of hydrocarbon migration and accumulation, one during the Late Triassic and the other during the Middle Jurassic–Cretaceous.
The chemical processes leading to magnetic mineral formation in the presence of hydrocarbons is complex, and depends on the complex interplay between the host reservoir rocks, sulfur content of the hydrocarbons, origin of the hydrocarbons, the redox conditions and temperature/depth of remagnetization (Machel, 1995; Badejo et al., 2021: Abdulkarim et al., 2022; Perkins, 2022). Generally, hydrocarbons produce reductive environments leading to the formation of iron sulphides (Machel, 1995; Zhang et al., 2018), however, in very low-sulfur hydrocarbon environments, magnetite formation has been widely observed and reported (e.g. Perkins, 2022). Perkins (2022) suggest that the magnetite is formed in relatively small quantities during the dehydroxylation of goethite to hematite, however, given magnetite's relatively strong magnetic properties, it dominates the NRM.

5.2 Linking Re–Os isotope ages to hydrocarbon evolution

Rhenium–Os data from crude oil in the remagnetized carbonates yielded an absolute age of 93.8 ± 9.8 Ma (Figure 7a), which indicates that hydrocarbon evolution reset the Re–Os system. Two potential mechanisms which are thought to reset the Re–Os geochronometer are oil generation (e.g., Cumming et al., 2014; Georgiev et al., 2016; Selby & Creaser, 2005) and hydrothermal alteration (e.g., Lillis & Selby, 2013). Given that the $^{87}Sr/^{86}Sr$ isotope compositions of the Permian carbonate rocks are within the isotopic range of Permian seawater, significant hydrothermal alteration of crude oil seems to be less likely. Recent geochemical analysis of the same reservoir, also found no evidence for hydrothermal alteration (Xiao et al., 2021). Oil generation is therefore suggested as the most likely origin of crude oil Re–Os age.

The bitumen samples show a Re–Os age of 264 ± 16 Ma (Figure 7b). As bitumen is a secondary product that evolves from liquid oil following oil generation and migration, various formation mechanisms are possible. These mechanisms are generally divided into two categories: 1) thermal cracking resulting in pyrobitumen marked by higher vitrinite reflectance values, and 2) mechanisms unconnected to thermal cracking such as water washing and biodegradation (Jacob 1985; Larter et al., 2006; Li et al., 2020; Mastalerz et al., 2018; Shalaby et al., 2012). Neither water washing nor biodegradation was considered to notably influence Re–Os isotope systematics (Finlay et al., 2011; Lillis & Selby, 2013; Selby et al., 2005). Additionally, post-accumulation disturbances that chemically react with hydrothermal fluids can alter Re–Os systematics (Lillis & Selby, 2013); however, using the same reasoning given above for oil, we dismiss hydrothermal alteration as a likely origin of bitumen Re–Os age. Therefore, bitumen Re–Os ages are primarily associated with oil generation and thermal cracking (Ge et al., 2016; Selby et al, 2005). Of the two remaining possible mechanisms, we suggest that the oil generation is the most likely, because the vitrinite reflectance data for the bitumen samples are generally lower than those for gas generation and oil cracking (Ro＞1.3; Mastalerz et al., 2018).

5.3 Combined remagnetization and Re–Os isotopes age analysis

It is likely that the Re–Os ages for the hydrocarbon samples and the remagnetization data for the hydrocarbon-bearing carbonate yield ages are related to the same process of hydrocarbon evolution. In this natural process, the hydrocarbon generation should occur prior to or coeval with hydrocarbon accumulation, and the oil cracking and hydrothermal alteration should occur after oil accumulation. Therefore, we determined that the age of earlier oil generation is ~264 Ma based on the Re–Os age of bitumen, which agrees with the oil accumulation age during the Late Triassic based on the remagnetization ChRM-1 (Figure 11). Similarly, the second oil-generation age based on the Re-Os data for crude oil is ~94 Ma, which agrees with the broad age range for ChRM-2, i.e., covering the Middle Jurassic–Cretaceous. This combined study can now limit the age range into the Late Cretaceous. ChRM-2 is broad because of overlapping pole positions for the APWP of South China during Middle Jurassic–Cretaceous (Figure 2g).

By using the combined method, we can track two periods of hydrocarbon evolution, even without prior knowledge of the source rocks and complexity of the system. In the first stage, the oil generated at the age of ~264 Ma and possibly migrated into an initial reservoir. Until the Late Triassic, the oil subsequently migrated into the Permian reservoir rocks studied here. In the second stage, another generation of oil occurred at the age of ~94 Ma, which migrated and then was trapped in the same Permian reservoir. These new ages are big improvements on previous age estimates for hydrocarbon evolution in the Longmen Shan belt, based mainly on basin models, which themselves rely on often poorly constrained parameters such paleo-heat flow, strata thickness *etc.* (Li et al., 2022; Lu et al., 2017; Luo et al., 2020; Qiu et al., 2021). These poorly constrained models yield a wide range of hydrocarbon evolution ages from the Permian to Paleogene, although there is a consensus on three characteristics: (1) multiple hydrocarbon activities have occurred; (2) a secondary migration for the earlier hydrocarbon activity happened; (3) faults are the primary migration pathways.

5.4 Hydrocarbon evolution and tectonic events in the studied regions

Hydrocarbon generation and accumulation is a dynamic process relying on depth and temperature, and pathways and trapping, all of which can be related to tectonic events (Philippi, 1965). Here we link hydrocarbon evolution to three phases of tectonism mainly based on temporal links and the results of the fold test (Figures 3, 4 and 11). Firstly, our study shows hydrocarbons were initially generated at~260 Ma, which is similar in age to the ~260 Ma Dongwu large igneous province which occurred around the Sichuan Basin (Li et al., 2015; Shellnutt, 2014). It is very likely that the study region was significantly influenced by this thermal event, leading to the oil generation. This is supported by U–Pb ages for nearby diabase dykes (~261 Ma; Shen et al., 2018). Secondly, based on the negative fold test (Figures 3 and 4), we suggest that the Late Triassic Indosinian thrusting would have faulted and folded the region to form the suitable migration paths and entrapment structures, e.g., the Changjianggou and Chejiaba folds (Yan et al., 2011). These Indosinian event connected the initial reservoir through faults, resulting in the hydrocarbon's secondary migration and accumulation in the studied Permian reservoir.

Thirdly, continued thrusting during the Cretaceous Yanshan event led to subsidence of the adjacent foreland basin (Li et al., 2012), increasing burial depth and temperature promoting a second phase of oil generation at 94 ± 10 Ma. The oil was subsequently mobilized and trapped in the pre-existing folds formed by the Indosinian events, indicating that the Yanshan event may not significantly change the pre-existing folds, but have re-activated existing thrust faults to provide migration paths. The apatite fission track ages in the Longmen Shan belt also indicate that the Late Cretaceous was the most intense episode of the Yanshan orogeny (Li et al., 2012; Xu, et al., 2018).

In summary, although the northern portion of Longmen Shan orogen records extensive superimposed tectonism, it is during the Indosinian tectonic event that the main geological structures that allowed for migration and entrapment of hydrocarbon, formed. The Dongwu magmatism and Yanshan tectonism provided the heat for hydrocarbon maturation, and the latter may also have re-actived migration paths. It is suggested that the Cenozoic Himalayan, which is thought to be significant in the formation of the Longmen Shan belt (Li et al., 2014; Wang et al., 2013), did not significantly affect the hydrocarbons in the region.

6. Conclusion

A combination of paleomagnetic and Re–Os isotope data acquisition and analysis has been conducted on a complex carbonate reservoir in the northern portion of the Longmen Shan belt. With the new data we determined the sequence of hydrocarbon evolution, from generation to migration to accumulation, and we relate these processes to regional orogenesis. We show that there are two periods of hydrocarbon generation at ~264 Ma and ~94 Ma, the former associated with the ~260 Ma Dongwu large igneous province, and the latter with the Yanshan orogenic events; there are also two periods of hydrocarbon accumulation during the Late Triassic and Cretaceous, the former associated with the Late Triassic Indosinian orogeny. Such geochronological information can be used to calibrate uncertain basin modelling parameters, and reduce uncertainty associated with exploration in the future.

Due to other possible mechanisms of remagnetization and resetting of Re–Os isotope systems, including hydrocarbon generation, cracking and hydrothermal alteration, combining these two methods has the potential to constrain a range of critical hydrocarbon processes, providing more credible information than a single method alone. The combined methods employed here should be applicable globally, when: 1) complex hydrocarbon evolution process need to be characterized, especially without a firm understanding of geological settings, and 2) the interpretation of each single method needs to be strengthened.

Acknowledgments

We would like to express our gratitude to Shuxin Shen, Jingping Zi, Xuzhi Hu, Geoff Nowell, and Chris Ottley for their assistance during field and experimental work. Funding: This study was funded by the National Science Foundation of China (U22B6002; 42272235; 41902206); Foundation of Chinese Academy of Science (E22117).

Data Availability Statement

The data for this work could be downloaded on the website of https://doi.org/10.6084/m9.figshare.21905895.

References

Abdulkarim, M.A., Muxworthy, A.R., Fraser, A., Sims, M., Cowan, A., 2022. Effect of Hydrocarbon Presence and Properties on the Magnetic Signature of the Reservoir Sediments of the Catcher Area Development Region, UK North Sea. Front. Earth Sci. 10, doi: 10.3389/feart.2022.818624.

Badejo, S. A., Muxworthy, A. R., Fraser, A., Neumaier, M., Perkins, J. R., Stevenson, G. R., & Davey, R. (2021). Using magnetic techniques to calibrate hydrocarbon migration in petroleum systems modelling: A Case Study from the Lower Tertiary, UK Central North Sea. *Geophysical Journal International*, *227*(1), 617–631. https://doi.org/10.1093/gji/ggab236

Bhullar, A. G., Karlsen, D. A., Backer-Owe, K., Seland, R. T., & Le Tran, K. (1999). Dating reservoir filling: a case history from the North Sea. *Marine and Petroleum Geology*, *16*(7), 581–603. https://doi.org/10.1016/S0264-8172(99)00028-8

Burchfiel, B. C., Chen, Z. L., Liu, Y. P., & Royden, L. H. (1995). Tectonics of the Longmen Shan and adjacent regions, central China. *International Geology Review*, *37*(8), 661–735. https://doi.org/10.1080/00206819509465424

Cumming, V. M., Selby, D., Lillis, P. G., & Lewan, M. D. (2014). Re–Os geochronology and Os isotope fingerprinting of petroleum sourced from a Type I lacustrine kerogen: Insights from the natural Green River petroleum system in the Uinta Basin and hydrous pyrolysis experiments. *Geochimica et Cosmochimica Acta*, *138*, 32–56. https://doi.org/10.1016/j.gca.2014.04.016

Dong, S., Zhang, Y., Li, H., Shi, W., Xue, H., Li, J., Huang, S., & Wang, Y. (2018). The Yanshan orogeny and late Mesozoic multi-plate convergence in East Asia—Commemorating 90th years of the “Yanshan Orogeny”. *Science China Earth Sciences*, *61*(12), 1888–1909. https://doi.org/10.1007/s11430-017-9297-y

Elmore, R. D., Engel, M. H., Crawford, L., Nick, K., Imbus, S., & Sofer Z. (1987). Evidence for a relationship between hydrocarbons and authigenic magnetite. *Nature*, *325*(6103), 428–430. https://doi.org/10.1038/325428a0

Elmore, R. D., & Leach, M. C. (1990). Remagnetization of the Rush Springs Formation, Cement, Oklahoma: Implications for Dating Hydrocarbon Migration and Aeromagnetic Exploration. *Geology*, *18*(2), 124–127. https://doi.org/10.1130/0091–7613(1990)018<0124:ROTRSF>2.3.CO;2

Elmore, R. D., Muxworthy, A. R., & Aldana, M. (2012). Remagnetization and chemical alteration of sedimentary rocks. *Geological Society, London, Special Publications*, *371*(1), 1–21. https://doi.org/ 10.1144/SP371.15

Emmerton, S., Muxworthy, A. R., & Sephton, M. A. (2012). Magnetic characterization of oil sands at Osmington mills and Mupe bay, Wessex Basin, UK. *Geological Society, London, Special Publications*, *371*(1), 189–198. https://doi.org/10.1144/sp371.6

Emmerton, S., Muxworthy, A. R., Sephton, M. A., Aldana, M., Costanzo-Alvarez, V., Bayona, G., & Williams, W. (2013). Correlating biodegradation to magnetization in oil bearing sedimentary rocks. *Geochimica et Cosmochimica Acta*, *112*, 146–165. https://doi.org/10.1016/j.gca.2013.03.008

Enkin, R. J. (1994). A computer program package for analysis and presentation of paleomagnetic data. *Pacific Geoscience Centre, Geological Survey of Canada*, *16*, 1–16.

Enkin, R. J. (2003). The direction–correction tilt test: an all-purpose tilt/fold test for paleomagnetic studies. *Earth and Planetary Science Letters*, *212*(1), 151–166. https://doi.org/10.1016/S0012-821X(03)00238-3

Finlay, A. J., Selby, D., & Osborne, M. J. (2011). Re-Os geochronology and fingerprinting of United Kingdom Atlantic margin oil: Temporal implications for regional petroleum systems. *Geology*, *39*(5), 475-478. https://doi.org/10.1130/G31781.1

Gao, G., Cao, J., Luo, B., Xiao, D., Zhang, Y., & Chen, C. (2020). Evidence of the Middle Permian marine mixed type source rocks in the northwestern Sichuan Basin and its contribution to large gas reservoirs in Shuangyushi area. *Acta Petrolei Sinica*, *41*(4), 433–445. https://doi.org/10.7623/syxb202004006

Ge, X., Shen, C. B., Selby, D., Deng, D. F., & Mei, L. F. (2016). Apatite fission-track and Re–Os geochronology of the Xuefeng uplift, China: Temporal implications for dry gas associated hydrocarbon systems. *Geology*, *44*(6), 491–494. https://doi.org/10.1130/G37666.1

Georgiev, S. V., Stein, H. J., Hannah, J. L., Galimberti, R., Nali, M., Yang, G., & Zimmerman A. (2016). Re–Os dating of maltenes and asphaltenes within single samples of crude oil. *Geochimica Et Cosmochimica Acta*, *179*, 53–75. https://doi.org/10.1016/j.gca.2016.01.016

He, B., Xu, Y. G., Huang, X. L., Luo, Z. Y., Shi, Y. R., Yang, Q. J., & Yu, S. Y. (2007). Age and duration of the Emeishan flood volcanism, SW China: geochemistry and SHRIMP zircon U–Pb dating of silicic ignimbrites, post-volcanic Xuanwei Formation and clay tuff at the Chaotian section. *Earth Planetary Science Letters*, *255*(3–4), 306–323. https://doi.org/10.1016/j.epsl.2006.12.021

Heller, F., Lowrie, W., Li, H., & Junda, W. (1988). Magnetostratigraphy of the Permo-Triassic boundary section at Shangsi (Guangyuan, Sichuan Province, China). *Earth and Planetary Science Letters*, *88*(3–4), 348–356. https://doi.org/10.1016/0012-821X(88)90091-X

Hu, G., He, F., Mi, J., Yuan, Y., & Guo, J. (2021). The geochemical characteristics, distribution of marine source rocks and gas exploration potential in the northwestern Sichuan Basin, China. *Journal of Natural Gas Geoscience*, *6*(4), 199–213. https://doi.org/10.1016/j.jnggs.2021.07.004

Jacob, H. (1985). Disperse solid bitumens as an indicator for migration and maturity in prospecting for oil and gas. *Erdoel Kohle, Erdgas, Petrochem*, *38*(8), 365–374.

Jia, D., Wei, G., Chen, Z., Li, B., Zeng, Q., & Yang, G. (2006). Longmen Shan fold-thrust belt and its relation to the western Sichuan Basin in central China: New insights from hydrocarbon exploration. *AAPG Bulletin*, *90*(9), 1425–1447. https://doi.org/10.1306/03230605076

Kirschvink, J. (1980). The least-squares line and plane and the analysis of paleomagnetic data. *Geophysical Journal International*, *189*, 269–276. https://doi.org/10.1111/j.1365-246X.1980.tb02601.x

Kruiver, P. P., Dekkers, M. J., & Heslop, D. (2001). Quantification of magnetic coercivity components by the analysis of acquisition curves of isothermal remanent magnetisation. *Earth and Planetary Science Letters*, *189*(3–4), 269–276. https://doi.org/10.1016/S0012-821X(01)00367-3

Larter, S., Huang, H., Adams, J., Bennett, B., Jokanola, O., Oldenburg, T., Jones, M., Head, I., Riediger, C., & Fowler, M. (2006). The controls on the composition of biodegraded oils in the deep subsurface: Part II—Geological controls on subsurface biodegradation fluxes and constraints on reservoir-fluid property prediction. *AAPG bulletin,* *90*(6), 921–938. https://doi.org/10.1306/01270605130

Li, B., Zhang, X., Mei, W., Zhao, Z., & Xin, J. (2022). Burial and thermal history simulation of Paleozoic source rocks in the northwest Sichuan Basin: implications for hydrocarbon generation

and charging history. *Environmental Earth Sciences, 81*(4), 1–16. https://doi.org/10.1007/s12665-022-10254-7
Li, H., & Wang, J. (1989). Magnetostratigraphy of Permo-Triassic boundary section of Meishan of Changxing, Zhejiang. *Science in China Ser B*, *32*(11), 1401–1408.
Li, H., Zhang, Z., Ernst, R., Lü, L., Santosh, M., Zhang, D., & Cheng, Z. (2015). Giant radiating mafic dyke swarm of the Emeishan Large Igneous Province: Identifying the mantle plume centre. *Terra Nova*, *27*(4), 247–257. https://doi.org/10.1111/ter.12154
Li, Y., Chen, S., Wang, Y., Su, K., He, Q., Qiu, W., & Xiao, Z. (2020). Relationships between hydrocarbon evolution and the geochemistry of solid bitumen in the Guanwushan Formation, NW Sichuan Basin. *Marine and Petroleum Geology*, *111*, 116–134. https://doi.org/10.1016/j.marpetgeo.2019.08.018
Li, Z., Jia, D., Chen, W., Yin, H., Shen, L., Sun, C., et al. (2014). Late Cenozoic east–west crustal shortening in southern Longmen Shan, eastern Tibet: Implications for regional stress field changes. *Tectonophysics*, *623*, 169–186. https://doi.org/10.1016/j.tecto.2014.03.033
Li, Z. W., Liu, S., Chen, H., Deng, B., Hou, M., Wu, W., & Cao, J. (2012). Spatial variation in Meso-Cenozoic exhumation history of the Longmen Shan thrust belt (eastern Tibetan Plateau) and the adjacent western Sichuan basin: Constraints from fission track thermochronology. *Journal of Asian Earth Sciences*, *47*, 185–203. https://doi.org/10.1016/j.jseaes.2011.10.016
Li, Z., Wang, X., Liu, K., Svetlana, T., Yang, X., Ma, X., & Sun, H. (2017). Rhenium-osmium geochronology in dating petroleum systems: Progress and challenges. *Acta Petrolei Sinica*, *38*(3), 297–306. https://doi.org/10.7623/syxb201703006
Lillis, P. G., & Selby, D. (2013). Evaluation of the rhenium–osmium geochronometer in the Phosphoria petroleum system, Bighorn Basin of Wyoming and Montana, USA. *Geochimica et Cosmochimica Acta*, *118*, 312–330. https://doi.org/10.1016/j.gca.2013.04.021
Lowrie, W. (1990). Identification of ferromagnetic minerals in a rock by coercivity and unblocking temperature properties. *Geophysical Research Letters*, *17*(2), 159–162. https://doi.org/10.1029/GL017i002p00159
Lu, J., Ma, J., Chen, S., Wu, B., Li, Y., Zhang, B., Han, H., & Lin, R. (2017). The geochemistry and origin of lower Permian gas in the northwestern Sichuan basin, SW China. *Journal of Petroleum Science and Engineering*, *157*, 906–916. https://doi.org/10.1016/j.petrol.2017.07.068
Ludwig, K. (2008). Isoplot version 4.15: a geochronological toolkit for microsoft Excel. *Berkeley Geochronology Center, Special Publication*, *4*, 247–270.
Luo, B., Wen, L., Zhang, Y., Xie, C., Cao, J., Xiao, D., Guo, G., & Tan, X. (2020). Differential gas accumulation process of the Middle Permian Qixia Formation, Northwestern Sichuan Basin. *Oil Gas Geology*, *41*, 393–406. https://doi.org/10. 11743/ogg20200215
Machel, H. G. (1995). Magnetic mineral assemblages and magnetic contrasts in diagenetic environments – with implications for studies of paleomagnetism, hydrocarbon migration and exploration. *Geological Society, London, Special Publications*, *98*, 9–29. https://doi.org/10.1144/GSL.SP.1995.098.01.02
Manning, E.B., & Elmore, R.D. (2015). An integrated paleomagnetic, rock magnetic, and geochemical study of the Marcellus shale in the Valley and Ridge province in Pennsylvania and West Virginia. *Journal of Geophysical Research-Solid Earth*, *120*, 705–724. https://doi.org/10.1002/2014JB011418

Mastalerz, M., Drobniak, A., & Stankiewicz, A. B. (2018). Origin, properties, and implications of solid bitumen in source-rock reservoirs: a review. *International Journal of Coal Geology*, *195*, 14–36. https://doi.org/10.1016/j.coal.2018.05.013

McArthur, J., Howarth, R. & Shields, G. A. (2012). Strontium isotope stratigraphy. *The Geologic Time Scale* (pp. 127–144). Boston: Elsevier.

Perkins, J. R. (2022). Hydrocarbon source and migration pathway identification through basin and petroleum systems modelling and mineral magnetism: a case study on the Beatrice Field, Inner Moray Firth, UK North Sea (Doctoral dissertation). London, UK: Imperial College London.

Philippi, G. T. (1965). On the depth, time and mechanism of petroleum generation. *Geochimica et Cosmochimica Acta, 29*(9), 1021–1049, https://doi.org/10.1016/0016-7037(65)90101-8

Qiu, N., Liu, W., Fu, X., Li, W., Xu, Q., & Zhu, C. (2021). Maturity evolution of Lower Cambrian Qiongzhusi Formation shale of the Sichuan Basin. *Marine and Petroleum Geology*, *128*, 105061. https://doi.org/10.1016/j.marpetgeo.2021.105061

Selby, D., & Creaser, R. A. (2005). Direct radiometric dating of hydrocarbon deposits using rhenium–osmium isotopes. *Science*, *308*(5726), 1293–1295. https://doi.org/10.1126/science.1111081

Selby, D., Creaser, R., Dewing, K., & Fowler, M. (2005). Evaluation of bitumen as a Re–Os geochronometer for hydrocarbon maturation and migration: A test case from the Polaris MVT deposit, Canada. *Earth and Planetary Science Letters*, *235*(1–2), 1–15. https://doi.org/10.1016/j.epsl.2005.02.018

Shalaby, M. R., Hakimi, M. H., & Abdullah, W. H. (2012). Geochemical characterization of solid bitumen (migrabitumen) in the Jurassic sandstone reservoir of the Tut Field, Shushan Basin, northern Western Desert of Egypt. *International Journal of Coal Geology*, *100*, 26–39. https://doi.org/10.1016/j.coal.2012.06.001

Shellnutt, J. G. (2014). The Emeishan large igneous province: a synthesis. *Geoscience Frontiers*, *5*(3), 369–394. https://doi.org/10.1016/j.gsf.2013.07.003

Shen, S., Jia, D., Zeng, Q., Xie, C., Zi, J., Zhang, Y., & Hu, J. (2018). Baddeleyite U-Pb geochronology of Maliucun Diabase from Tangwangzhai-Yangtianwo syncline in the northern segment of Longmen Mountain, Sichuan, and its geological significance. *Geological Bull. of China, 37*, 840–852.

Smoliar, M., Walker, R., & Morgan, J. (1996). Re-Os isotope constraints on the age of Group IIA, IIIA, IVA, and IVB iron meteorites. *Science*, *271*, 1099–1102.

Steiner, M., Ogg, J., Zhang, Z., & Sun, S. (1989). The Late Permian/Early Triassic magnetic polarity time scale and plate motions of South China. *Journal of Geophysical Research: Solid Earth*, *94*(B6), 7343–7363. https://doi.org/10.1029/JB094iB06p07343

Tan, K., Li, Y., Liao, J., Xu, Z., Liu, Z., & Lin, Z. (2022). The origin and source of natural gas in the Lower Permian in Hewanchang area, Northwest Sichuan. *Arabian Journal of Geosciences*, *15*(1), 1–9. https://doi.org/10.1007/s12517-021-08890-7

Tauxe, L., Shaar, R., Jonestrask, L., Swanson-Hysell, N. L., Minnett, R., Koppers, A. A. P., et al. (2016). PmagPy: Software package for paleomagnetic data analysis and a bridge to the Magnetics Information Consortium (MagIC) Database. *Geochemistry, Geophysics, Geosystems*, *17*(6), 2450–2463. https://doi.org/10.1002/2016GC006307

Tauxe, L., & Watson, G. S. (1994). The fold test: an eigen analysis approach. *Earth and Planetary Science Letters*, *122*(3), 331–341. https://doi.org/10.1016/0012-821X(94)90006-X

Wang, E., Kirby, E., Furlong, K. P., Van Soest, M., Xu, G., Shi, X., Kamp, P. J., & Hodges, K. J. N. G. (2012). Two-phase growth of high topography in eastern Tibet during the Cenozoic. *Nature Geoscience*, *5*(9), 640–645. https://doi.org/10.1038/NGEO1538

Wang, M., Jia, D., Shaw, J. H., Hubbard, J., Lin, A., Li, Y., & Shen, L. (2013). Active Fault-Related Folding beneath an Alluvial Terrace in the Southern Longmen Shan Range Front, Sichuan Basin, China: Implications for Seismic Hazard. *Bulletin of the Seismological Society of America, 103*(4), 2369–2385. https://doi.org/10.1785/0120120188

Wang, W. Q., Garbelli, C., Zheng, Q. F., Chen, J., Liu, X. C., Wang, W., & Shen, S. Z. (2018). Permian $^{87}Sr/^{86}Sr$ chemostratigraphy from carbonate sequences in South China. *Palaeogeography, Palaeoclimatology, Palaeoecology*, *500*, 84–94. https://doi.org/10.1016/j.palaeo.2018.03.035

Xiao, D., Wen, L., Zhang, Y., Xie, C., Tan, X., & Cao, J. (2021). Natural gas accumulation in the basin–mountain transition zone, northwestern Sichuan Basin, China. *Marine and Petroleum Geology*, *133*, 1–15. https://doi.org/10.1016/j.marpetgeo.2021.105305

Xie, Z., Yang, C., Dong, C., Dai, X., Zhang, L., Guo, J., Guo, Z., Li, Z., Li, J., & Qi, X. (2020). Geochemical characteristics and genesis of the Middle Devonian and the Middle Permian natural gas in the Sichuan Basin, China. *Journal of Natural Gas Geoscience*, *5*(4), 185–198. https://doi.org/10.11764/j.issn.1672-1926.2020.01.005

Xu, Q., Qiu, N., Liu, W., Shen, A., Wang, X., & Zhang, G. (2018). Characteristics of the temperature–pressure field evolution of Middle Permian system in the northwest of Sichuan Basin. *Energy Exploration & Exploitation*, *36*(4), 705–726. https://doi.org/10.1177/0144598717752148

Yan, D. P., Zhou, M. F., Li, S. B., & Wei, G. Q. (2011). Structural and geochronological constraints on the Mesozoic-Cenozoic tectonic evolution of the Longmen Shan thrust belt, eastern Tibetan Plateau. *Tectonics*, *30*(6), 1–24. https://doi.org/10.1029/2011TC002867

Yan, D. P., Qiu, L., Wells, M. L., Zhou, M. F., Meng, X., Lu, S., Zhang, S., Wang, Y., & Li, S. B. (2018). Structural and Geochronological constraints on the early Mesozoic North Longmen Shan Thrust Belt: Foreland fold-thrust propagation of the SW Qinling Orogenic Belt, Northeastern Tibetan plateau. *Tectonics*, *37*(12), 4595–4624. https://doi.org/10.1029/2018TC004986

Yang, Z., Sun, Z., Yang, T., & Pei, J. (2004). A long connection (750–380 Ma) between South China and Australia: paleomagnetic constraints. *Earth and Planetary Science Letters*, *220*(3–4), 423–434. https://doi.org/10.1016/S0012-821X(04)00053-6

Zhang, S., Li, H., Jiang, G., Evans, D. A. D., Dong, J., Wu, H., Yang, T., Liu, P., & Xiao, Q. (2015b). New paleomagnetic results from the Ediacaran Doushantuo Formation in South China and their paleogeographic implications. *Precambrian Research*, *259*, 130–142. https://doi.org/10.1016/j.precamres.2014.09.018

Zhang, Y., Jia, D., Muxworthy, A. R., Li, Y., Xia, B., Xie, Z., Hu, J., Zi, J., & Liu, W. (2018). The Chemical Remagnetization of Ediacaran Dolomite in the Taishan Paleo-Reservoir, South China. *Journal of Geophysical Research: Solid Earth*, *123*(8), 6161–6175. https://doi.org/10.1029/2018JB015547

Zhang, Y., Jia, D., Muxworthy, A. R., Zhang, Y., Li, Y., Yin, H., Chen, Z., Brzozowski, M. J., Li, W., & Wang, M. (2020). Fluid migration and widespread remagnetization in the Dabashan fold and thrust belt, China. *Journal of Geophysical Research: Solid Earth*, *125*(11). https://doi.org/10.1029/2020JB019989

Zhang, Y., Jia, D., Shen, L., Yin, H., Chen, Z., Li, H., Li, Z., & Sun, C. (2015a). Provenance of detrital zircons in the Late Triassic Sichuan foreland basin: constraints on the evolution of the Qinling

Orogen and Longmen Shan thrust-fold belt in central China. *International Geology Review*, *57*(14), 1806-1824. https://doi.org/10.1080/00206814.2015.1027967

Zhang, Y., Jia, D., Yin, H. W., Liu, M. C., Xie, W. R., Wei, G. Q., & Li, Y. X. (2016). Remagnetization of lower Silurian black shale and insights into shale gas in the Sichuan Basin, south China. *Journal of Geophysical Research: Solid Earth*, *121*, 491–505. https://doi.org/10.1002/2015JB012502

Zhang, Y., Muxworthy, A. R., Jia, D., Wei, G., Xia, B., Wen, B., Wang, M., Liu, W., & Brzozowski, M. J. (2019). Identifying and Dating the Destruction of Hydrocarbon Reservoirs Using Secondary Chemical Remanent Magnetization. *Geophysical Research Letters*, *46*, 11100–11108. https://doi.org/110.1029/2019gl084812

Table Captions

Table 1. Summary of site-mean ChRM directions of Permian shale and carbonate rocks from the northern portion of the Longmen Shan Belt. Strike/dip are the bedding as measured in the field (right hand rule), *N* is the number of directions used to determine the ChRM, *Dg* and *Ig* are the geographic declination and inclination, and *Ds* and *Is* the stratigraphic declination and inclination, *k* the precision parameter and α_{95} the standard confidence error.

Table 2. Rhenium–Osmium content and isotopic composition for oil and bitumen samples from Permian reservoir rocks, which paleomagnetic measurements were done. ppb = part per billion, ppt = part per trillion and rho = the associated error correlation.

Figure Captions

Figure 1. Simplified geological maps of: (a) China, (b) the Sichuan Basin and its surrounding blocks, PGF is the Puguang gas field. (c) The northern Longmen Shan belt, (d) a stratigraphic column of the western Sichuan Basin (modified from Jia et al., 2006). In (c) the distribution of Cambrian–Cretaceous units and faults are shown, in addition to the sampling locations for this study. Each sampling location symbol in the map contains 1–7 sampling sites, which are spaced tens of meters to several kilometers apart.

Figure 2. Paleomagnetic data: (a) progressive thermal demagnetization data of sample CJG5-5, which is a typical ChRM-1-bearing sample; (b) progressive alternating demagnetization data of sample CJB05-9-IS, which is a typical ChRM-2-bearing sample; (c) site–mean data in situ coordinates for ChRM-1-bearing samples; (d) site–mean data in situ coordinates for ChRM-2-bearing samples; (e) site–mean data in tilt-corrected coordinates for ChRM-1-bearing samples; (f) site–mean data in tilt-corrected coordinates for ChRM-2-bearing samples; (g) In the APWP of South China Block (Zhang et al., 2015b), virtual geomagnetic poles were plotted. In (a) and (b), the blue lines represent viscous remanent magnetization and the red (ChRM-1) and orange (ChRM-2) lines highlight the picked ChRM directions. In (c), (d) and (g), the red and orange stars denote the average directions of the ChRM-1 and ChRM-2, respectively.

Figure 3. Results for the progressive tilt test and direction-correction test (Enkin, 2003) of ChRM1 (a–b) and ChRM2 (c–d). In (a) and (c), the maximum value of precision parameter (K) occurs at ~0% untilting. In (b) and (d), the 95% confidence region constrained by the dashed lines do not coincide with black solid line, indicating a negative tilt test.

Figure 4. Results of the fold test using the approach of Tauxe and Watson (1994) for: (a) ChRM-1 samples and (b) ChRM-2 samples. The black line is the maximum eigenvalue as an unfolding function. The red lines are the boot-strapping estimates used to estimate the green line, which is the cumulative distribution function of the unfolding percentage. The blue lines are the 95% confidence boundaries for the green line.

Figure 5. (a–b) IRM acquisition curves of typical samples from the three folds and different lithologies as labeled in the legends; (c–h) typical IRM analysis charts through the approach of Kruiver et al. (2001). As exhibited are linear acquisition plot, gradient acquisition plot and standardized acquisition plot for (c) CJG01, (d) CJG02, (e) CJB04, (f) CJB07, (g) CJB08 and (h) ZY02. The data were listed in the Table S1, which were available on the website of https://doi.org/10.6084/m9.figshare.21905895.

Figure 6. Triaxial IRM thermal demagnetization curves of representative samples from three folds and different lithology: (a) CJG01, (b) CJG02, (c) CJB04, (d) CJB07, (e) CJB08 and (f) ZY02. Three perpendicular fields were applied before thermal demagnetization: 0.12 T, 0.4 T and 2.4 T. The coercivity value of soft fraction should be in the range of 0-0.12 T, the medium fraction is in the range of 0.12-0.4 T and the hard fraction is in the range of 0.4-2.4 T.

Figure 7. $^{187}Re/^{188}Os$ versus $^{187}Os/^{188}Os$ binary diagrams for oil (a) and bitumen (b) from Permian carbonate reservoir samples. Ellipses on data points represent 2σ absolute uncertainty. MSWD = mean squared weighted deviation. See Table 2 for the Re-Os data.

Figure 8. Backscatter electron images of representative Permian carbonate reservoir samples. Bitumen and iron oxide grains are distributed along fractures (a–c) and in pore spaces (d, e). The iron oxides often occur around the fractures, pores and bitumen. Typical EDS spectra for bitumen, magnetite and iron sulfides are depicted in figures (g)–(j); the locations are shown in (a)–(f).

Figure 9. NRM versus TOC for carbonate reservoir samples. A linear regression trend-line is plotted.

Figure 10. $^{87}Sr/^{86}Sr$ curves of Permian strata in this study and contemporaneous seawater. The orange lines exhibit the Sr isotope values for our representative samples. The black and yellow lines show the Sr isotope values of coeval seawater, which were modified from Wang et al. (2018) and McArthur et al. (2012). The grey and blue fields exhibit the Sr error scopes.

Figure 11. Relationship between hydrocarbon evolution and tectonic events, showing a comparison of the remagnetization time, Re–Os ages, U–Pb ages (Shen et al., 2018), ^{40}Ar–^{39}Ar (Yan et al., 2011) and apatite fission track ages (Li et al., 2012).

Figure 1.

105°15'E
105°30'E
105°45'E
32°30'N
32°10'N
Paleomagnetic sampling location
Re-Os sampling location (Oil)
Re-Os sampling location (Bitumen)
Fault
Cretaceous
Jurassic
Triassic
Ordovician–Cambrian
Permian
Carboniferous–Devonian
(c)
Longmen Shan Belt
Chejiaba (CJB)
Western Sichuan foreland basin
Well K1,3
Changjianggou (CJG)
Zhuyuan (ZY)
Well ST3
(a)
Tarim
Tibetan Plateau
NCB
SCB
Figure 1b
(b)
North China Block (NCB)
Qinling Orogen
Songpan-Gantz Belt
Longmen Shan
Figure 1c
Sichuan Basin
PGF
Qiangtang Block
South China Block (SCB)
N
Era
System& Formation
Age
Litho
Tectonic Event
Legend
(d)
Cenozoic
Mesozoic
Paleozoic
Proterozoic
Quaternary
Neogene
Paleogene
Cretaceous
Jurassic
Triassic
Permian
Changxing
Longtan
Maokou
Qixia
Liangshan
Carboniferous
Devonian
Silurian
Ordovician
Cambrian
Ediacaran
Pre-Ediacaran
2.6
23
66
145
201
252
260
299
359
419
444
485
539
635
Himalayan
Yanshan
Indosinian
Dongwu
Caledonian
Sandstones
Shales
Mudstone
Siltstones
Basalts
Conglomerates
Gypsum rock
Limestones
Granites
Gneisses
Source Rocks
Sampling Site
Uncomformity

Figure 2.

(a) NRM CJG05-5-IS
N
80°
120°
150°
180°
240°
W
Scale: 1e-4 A/m
270°
E
430°
Down
S
Up
(b) NRM CJB05-9-IS
N
3mT
6mT
9mT
12mT
15mT
W
Scale: 1e-4 A/m
30mT
E
Down
40mT
S
Up
(c)
In Situ
Dec = 41°
Inc = 47°
n = 13
k = 92
α95 = 4
270
(d)
In Situ
Dec = 18°
Inc = 48°
n = 10
k = 159
α95 = 4
90
(e)
Tilt-corrected
Dec = 43°
Inc = 48°
n = 13
k = 5
α95 = 20
270
180
(f)
Tilt-corrected
Dec = 44°
Inc = 49°
n = 10
k = 3
α95 = 34
90
180
(g)
Q-E
60°
K2
K1
P1
J3
J2
J1
P2
C1
T3
T1
D1-2
30°
T2
S2
180°
210°

Figure 3.

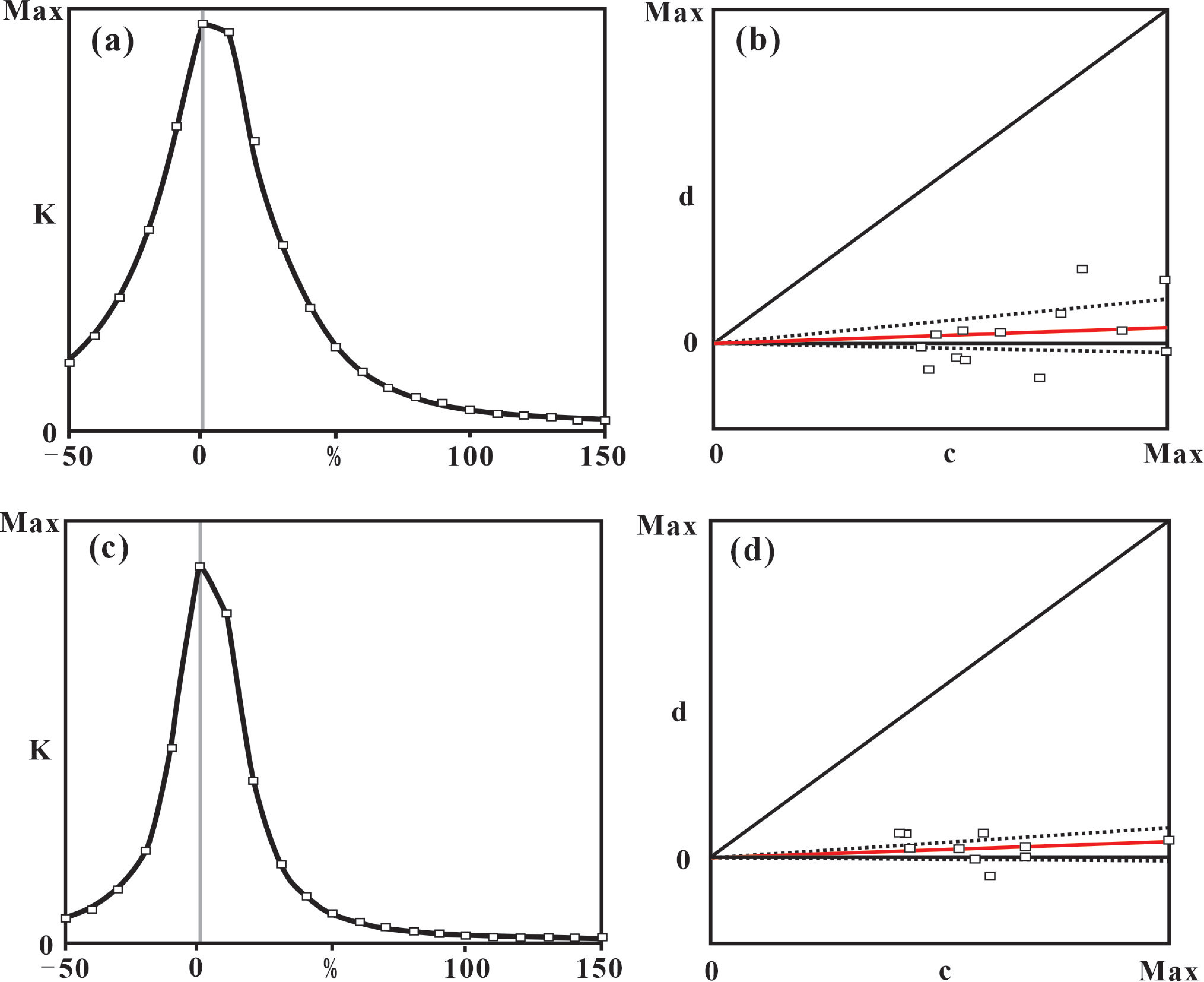

(a)
Max
K
0
−50
0
%
100
150
(b)
Max
d
0
0
c
Max
(c)
Max
K
0
−50
0
%
100
150
(d)
Max
d
0
0
c
Max

Figure 4.

(a)
-3 - 8 Percent Unfolding
tau_1 (red), CDF (green)
1.0
0.8
0.6
0.4
0.2
0.0
0
20
40
60
80
100
120
140
% Untilting
(b)
-1 - 7 Percent Unfolding
tau_1 (red), CDF (green)
1.0
0.8
0.6
0.4
0.2
0.0
0
20
40
60
80
100
120
140
% Untilting

Figure 5.

a) M/Mmax
IRM
Field (mT)
CJB01
CJB02
CJB03
CJB04
CJB07
CJB08
CJG01
CJG02
b) M/Mmax
IRM
Field (mT)
CJG03
CJG04
CJG05
CJG06
ZY01
ZY02
ZY05
ZY06
c) CJG01
Linear Acquisition Plot (LAP)
Gradient Acquisition Plot (GAP)
Standardised Acquisition Plot (SAP)
d) CJG02
e) CJB04
f) CJB07
g) CJB08
h) ZY02
LAP
GAP
SAP
IRM in A/m
Gradient in A/m
N
¹⁰Log Applied field in MT

Figure 6.

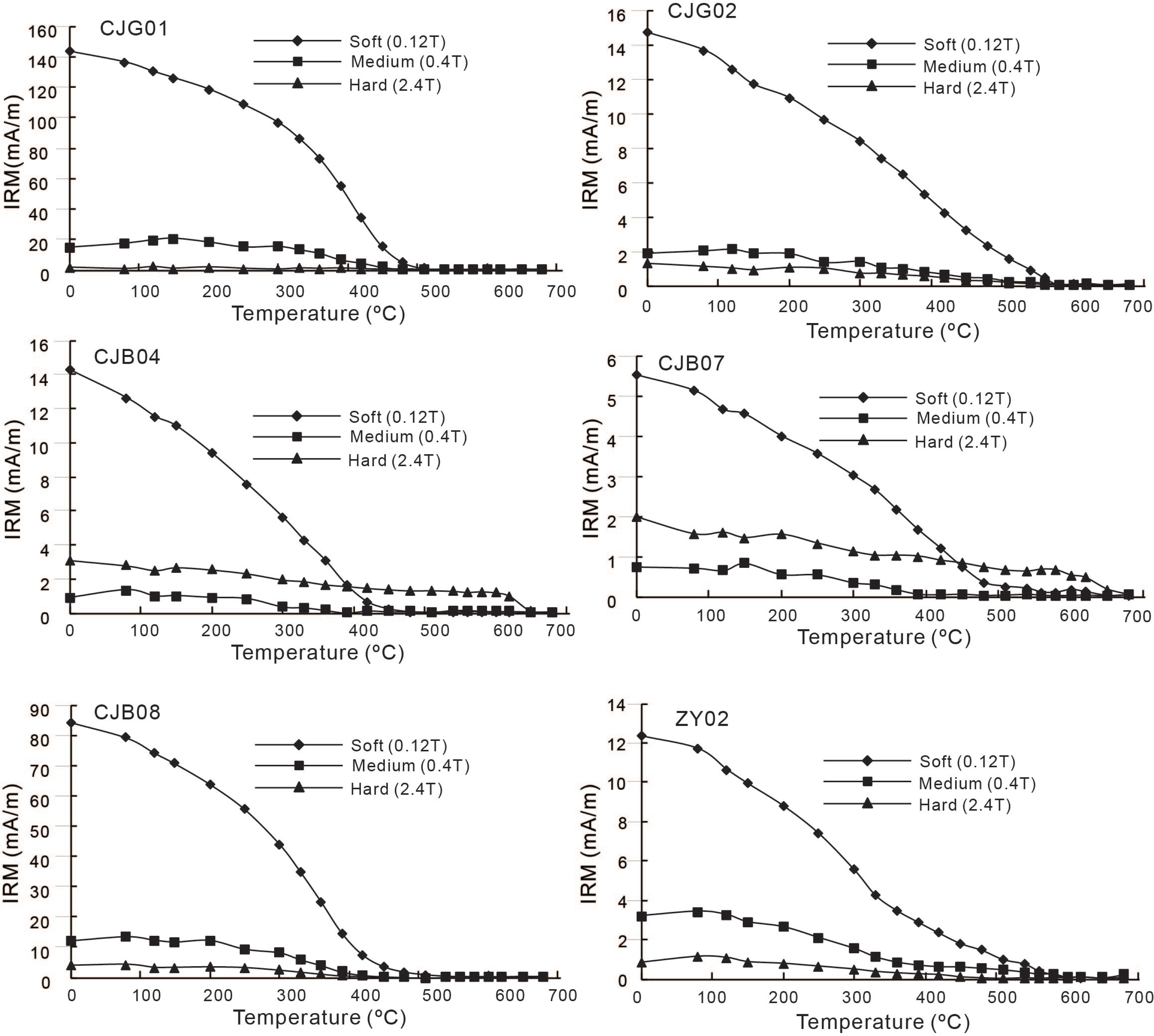
CJG01
Soft (0.12T)
Medium (0.4T)
Hard (2.4T)
IRM(mA/m)
Temperature (°C)
CJG02
Soft (0.12T)
Medium (0.4T)
Hard (2.4T)
IRM (mA/m)
Temperature (°C)
CJB04
Soft (0.12T)
Medium (0.4T)
Hard (2.4T)
IRM (mA/m)
Temperature (°C)
CJB07
Soft (0.12T)
Medium (0.4T)
Hard (2.4T)
IRM (mA/m)
Temperature (°C)
CJB08
Soft (0.12T)
Medium (0.4T)
Hard (2.4T)
IRM (mA/m)
Temperature (°C)
ZY02
Soft (0.12T)
Medium (0.4T)
Hard (2.4T)
IRM (mA/m)
Temperature (°C)

Figure 7.

a
Oil2
Oil1
Oil4
Oil3
Age=93.8±9.9
Os$_i$=0.994±0.061
MSWD=3.7
^{187}Os/^{188}Os
^{187}Re/^{188}Os
1.1
1.3
1.5
1.7
1.9
2.1
0
200
300
400
500
600
b
Age=268±17
Os$_i$=1.60±0.35
MSWD=541
(All bitumen data)
Bit-3
Bit-1
Bit-4
Bit-2
Bit-5
Bit-6~11
Age=264±16
Os$_i$=1.52±0.3
MSWD=42
(Bit-1, 2, 4, 6, 7 and 9)
0
4
8
12
16
1000
2000
3000

Figure 8.


(a)
Bitumen (g)
Pyrite (h)
Iron oxides (i)
10 μm
EHT = 15.00 kV Mag = 1.10 K X Signal A = AsB WD = 8.7 mm Supra 55
(b)
Bitumen (g)
Iron oxides (i)
2 μm
EHT = 15.00 kV Mag = 3.37 K X Signal A = AsB WD = 8.7 mm Supra 55
(c)
Bitumen (g)
Iron oxides (i)
10 μm
(d)
Iron oxides (i)
1 μm
EHT = 15.00 kV Mag = 3.59 K X Signal A = AsB WD = 8.8 mm Supra 55
(e)
Iron oxides (i)
1 μm
EHT = 15.00 kV Mag = 5.61 K X Signal A = AsB WD = 8.6 mm Supra 55
(f)
Iron sulfides (j)
5 μm
(g)
C
O
Si
S
Ca
(h)
S
C
Fe
Fe
Fe
(i)
O
C
Fe
Ca
Fe
(j)
S
O
C
Fe
Ca
Fe
Fe

Figure 9.

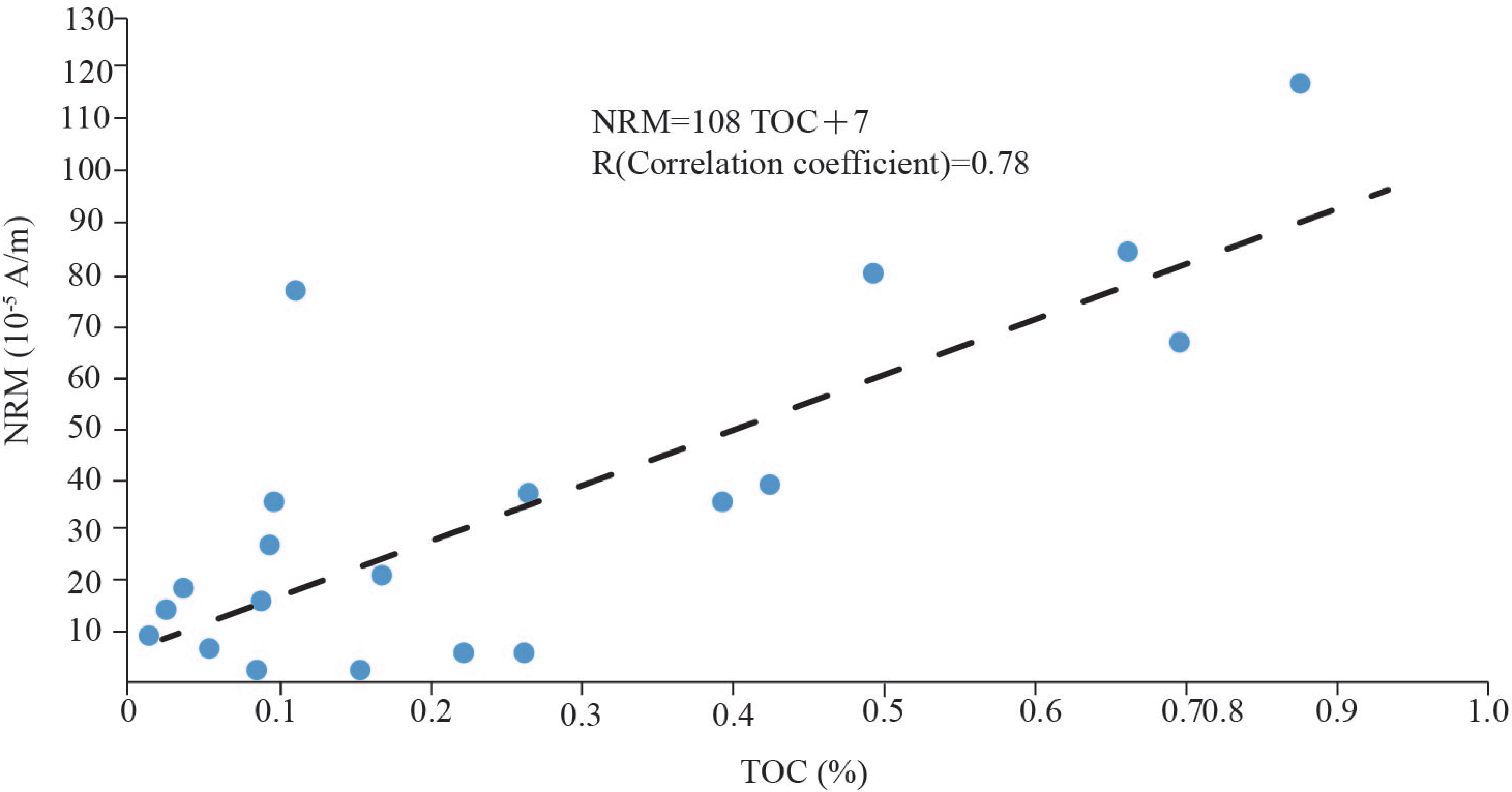
NRM=108 TOC+7
R(Correlation coefficient)=0.78
NRM (10^{-5} A/m)
TOC (%)
130
120
110
100
90
80
70
60
50
40
30
20
10
0
0.1
0.2
0.3
0.4
0.5
0.6
0.70.8
0.9
1.0

Figure 10.

Series
Stage
Age (Ma)
$^{87}Sr/^{86}Sr$
0.7070
0.7074
0.7078
0.7082
Lopingian
Guadalupian
Cisuralian
Wuchiapingian
Capitanian
Wordian
Roadian
Kungurian
Artinskian
Sakmarian
Asselian
255
260
265
270
275
280
285
290
295
ZY4-10

Figure 11.


Era
Permian
Triassic
Jurassic
Cretaceous
Cenozoic
Age(Ma)
280
260
240
220
200
180
160
140
120
100
80
60
40
20
Remagnetization Time
Late Triassic
Middle Jurassic-Cretaceous
Re-Os Age
264±16 Ma
Bitumen
93.8±9.8 Ma
Crude Oil
Tectonic Event
Shen et al., 2018
Yan et al., 2011
Li et al., 2012
261±2 Ma
U-Pb
237-208 Ma
^{40}Ar-^{39}Ar
109-80 Ma
Apatite fission track

Table 1. Summary of site-mean ChRM directions of Permian shale and carbonate rocks from the northern portion of the Longmen Shan Belt. Strike/dip are the bedding as measured in the field (right hand rule), *N* is the number of directions used to determine the ChRM, *Dg* and *Ig* are the geographic declination and inclination, and *Ds* and *Is* the stratigraphic declination and inclination, *k* the precision parameter and α_{95} the standard confidence error.

Site	Location	Lithology	Strike/dip (°)	ChRM	*N*	*Dg* (°)	*Ig* (°)	*Ds* (°)	*Is* (°)	*k*	α_{95} (°)
				Changjianggou Fold							
CJG01	32.321°N, 105.453°E	Limestone	33/33	ChRM-1	7	49	54	79	35	17	15
CJG02	32.324°N, 105.452°E	Limestone	32/40	ChRM-1	7	40	53	73	37	28	12
CJG03	32.297°N, 105.390°E	Limestone	215/36	ChRM-1	6	40	52	0	42	36	11
CJG04	32.288°N, 105.396°E	Limestone	215/36	ChRM-1	4	44	47	8	40	38	15
CJG05	32.290°N, 105.398°E	Limestone	215/42	ChRM-1	7	44	47	3	38	37	10
CJG06	32.293°N, 105.390°E	Limestone	229/82	ChRM-2	7	23	42	3	-13	48	9
				Chejiaba Fold							
CJB01	32.534°N, 105.739°E	Limestone	71/66	ChRM-1	7	49	32	95	32	35	10
CJB02	32.534°N, 105.739°E	Limestone	71/66	ChRM-2	6	21	43	111	53	107	7
CJB03	32.534°N, 105.739°E	Limestone	77/57	ChRM-1	6	32	48	115	53	32	12
CJB04	32.534°N, 105.739°E	Limestone	77/57	ChRM-2	7	18	46	115	63	86	7
CJB05	32.534°N, 105.739°E	Dolomite	73/66	ChRM-2	11	16	52	129	52	57	6
CJB06	32.534°N, 105.739°E	Dolomite	73/66	ChRM-1	8	35	51	120	43	29	11
CJB07	32.526°N, 105.741°E	Limestone	82/48	ChRM-1	6	35	44	100	60	62	9
CJB08	32.520°N, 105.750°E	Limestone	215/36	ChRM-2	13	16	56	346	33	50	6
CJB09	32.511°N, 105.754°E	Limestone	235/34	ChRM-1	10	39	42	17	27	51	7
CJB10	32.511°N, 105.754°E	Dolomite	234/26	ChRM-1	11	38	55	9	40	98	5
				Zhuyuan Fold							
ZY01	32.221°N, 105.292°E	Limestone	213/49	ChRM-2	11	20	53	344	25	109	4
ZY02	32.221°N, 105.292°E	Limestone	213/49	ChRM-1	8	33	48	353	30	137	5
ZY03	32.220°N, 105.292°E	Limestone	219/46	ChRM-2	8	18	55	346	23	83	6
ZY04	32.218°N, 105.285°E	Limestone	232/54	ChRM-1	9	53	36	23	21	39	8
ZY05	32.205°N, 105.299°E	Limestone	39/64	ChRM-2	7	20	39	71	31	37	10
ZY06	32.204°N, 105.312°E	Limestone	36/64	ChRM-2	8	11	46	75	36	127	5
ZY07	32.204°N, 105.312°E	Limestone	44/64	ChRM-2	8	14	47	85	39	88	6

Table 2. Rhenium–Osmium content and isotopic composition for oil and bitumen samples from Permian reservoir rocks, which paleomagnetic measurements were done. ppb = part per billion, ppt = part per trillion and rho = the associated error correlation.

Batch/Sample	Re (ppb)	±	Os (ppt)	±	$^{187}Re/^{188}Os$	±	$^{187}Os/^{188}Os$	±	rho
Oil1	13.6	0.04	241.5	1.6	319.3	2.6	1.507	0.015	0.704
Oil2	46.8	0.12	492.1	2.6	562.7	3.0	1.869	0.012	0.660
Oil3	21.1	0.06	600.6	3.0	194.8	1.2	1.293	0.009	0.650
Oil4	8.4	0.03	198.0	1.5	238.2	2.7	1.361	0.019	0.722
Bitumen-1	32.3	0.08	196.0	1.9	1752.5	15.1	9.356	0.086	0.861
Bitumen-2	15.2	0.04	97.3	1.4	1532.7	25.2	8.018	0.150	0.860
Bitumen-3	72.4	0.18	354.4	3.5	2903.6	21.0	15.082	0.121	0.794
Bitumen-4	22.1	0.06	144.1	1.6	1541.7	17.1	8.478	0.102	0.872
Bitumen-5	80.7	0.20	659.9	4.5	1000.4	4.8	5.468	0.031	0.616
Bitumen-6	13.6	0.04	443.5	2.8	190.4	1.2	2.322	0.018	0.650
Bitumen-7	12.2	0.03	423.1	2.7	179.1	1.1	2.371	0.019	0.654
Bitumen-8	15.6	0.04	524.7	3.4	189.8	1.2	2.630	0.020	0.650
Bitumen-9	15.6	0.04	459.7	2.9	213.6	1.3	2.460	0.019	0.657
Bitumen-10	18.3	0.05	669.0	4.3	173.9	1.0	2.593	0.020	0.647
Bitumen-11	7.7	0.02	476.5	4.1	102.5	1.0	2.579	0.032	0.676